



# A Numerical Study on the Seismic Response of RC Wide Column–Beam Joints

Hamed Dabiri<sup>1</sup> · Ali Kheyroddin<sup>2</sup> · Ahmad Kaviani<sup>1</sup>

Received: 10 May 2018 / Revised: 12 October 2018 / Accepted: 15 October 2018 / Published online: 1 November 2018  
© Iran University of Science and Technology 2018

## Abstract

Reinforced concrete (RC) column–beam joints are one of the most critical elements in RC structures which have a big impact on the seismic response of structures under different loads. To investigate the effect of beam and column dimensions on the seismic behavior of RC wide column–beam joints, 27 numerical models were created using nonlinear finite element method (FEM) software. Displacement-control condition was applied to the top surface of columns in all of the models and boundary conditions and material properties were considered the same as the experimental model. Three numerical models were verified by similar experimental study. The other models were changed in width and depth to find the effect of dimension changes on the displacement ductility and curvature ductility by evaluating force–displacement and moment–curvature diagrams. In general, it could be concluded that by increasing the ratio of beam width to beam height, displacement ductility of RC joint and curvature ductility of beam increase. Moreover, based on the FE analysis by increasing the ratio of column width to column height, displacement ductility increases, while curvature ductility decreases. Results also indicated that increasing the area of column section could lead to increase in displacement ductility and decrease in curvature ductility of RC wide column–beam joints. In addition, the influence of mesh size on the analytical outcome of FE analysis was also investigated. After evaluating the results, equations for estimating seismic parameters, displacement ductility and curvature ductility, in RC wide column–beam joints were suggested.

**Keywords** Reinforced concrete · Wide column–beam joint · Finite element · Displacement ductility · Curvature ductility

## 1 Introduction

Reinforced concrete moment resisting frames have been used as structural systems in buildings. They can have an acceptable response to seismic loads if designed properly. Beam–column connections play an important role in seismic behavior of structures, thus they become critical components [1]. In general, the width of beams and columns is chosen the same owing to easiness in construction. Wide columns in RC

structures, however, have become a norm because of structural limitations. Hence RC wide column–beam joints have become the center of researchers' attention and some studies have been carried out to evaluate the seismic performance of RC column–beam joints [1–10, 12–21]. In 2002, Li et al. carried out an experimental study on the seismic behavior of non-seismically detailed interior beam-wide column joints. The study presented the results of four full-scale RC interior beam-wide column joints; two of which were of wide column moment-resistance frames designed based on BS 110, and the other two models were changed in reinforcement and were made to be compared with the as-built ones. The two variables in this study were the amount of joint transverse reinforcement and the lap splice details for column and beam reinforcement. The study did not result in desirable values in parameters including lateral load capacity, drift, stiffness and displacement ductility. Although the two as-built specimens failed at the low displacement ductility level, the other modified RC beam-wide column joints reached a limited displacement ductility level which led to improvement in

✉ Ali Kheyroddin  
kheyroddin@semnan.ac.ir

Hamed Dabiri  
hameddabiri@alum.semnan.ac.ir

Ahmad Kaviani  
ahmad\_kaviani@students.semnan.ac.ir

<sup>1</sup> Structural Engineering, Semnan University, Semnan, Iran

<sup>2</sup> Faculty of Civil Engineering, Semnan University, Semnan, Iran

the seismic behavior of the joints [12]. Another numerical research was carried out by Li et al. in 2003 discussing the global behavior and the principal stress of the interior beam-wide column joints. Results of the numerical study generally indicated that modifying the reinforcing details have no remarkable influence on the improvement of bond conditions, since the bond conditions mainly depend on the ratio of the beam and column main bar diameters to the depth of them. Moreover, this study showed that the impact of “bar diameter to column height ratio” on conventional joints is more than the wall-like column joints [13]. To investigate the seismic behavior of non-seismically detailed interior beam-wide columns and beam-wall joints, a research was done by Li et al. in 2009. Six full-scale non-seismically detailed RC interior beam-wide column and beam-wall joints with zero to high axial compression loads were tested. Lateral load capacity, drift, energy dissipation capacity, stiffness and nominal joint shear stress were examined. The conclusion of the experimental study was that RC interior beam-wide column joints and beam-wall joints with non-seismic design and detailing, attained a drift ratio of 2% with no significant strength degradation. The other point which was mentioned in the test results was that such joints could also possess inherent ductility for adequate response to unexpected moderate earthquakes [14, 15]. In 2009, Benavent-Climent et al. investigated the performance of exterior wide beam–column connections in existing RC frames in terms of strength, displacement, ductility and energy dissipation capacity [1]. A new design method for the joints particularly suitable for low to medium seismic effects in earthquake zones was introduced by Lu et al. experimental study in 2012. Results of this study showed that adding bars (diagonal and straight) can result in fewer cracks in the columns [16]. A numerical research for simulating inelastic and elastic behavior of RC beam–column connections was done by Omidi and Behnamfar in 2015. Their models were made of two main elements; a rigid offset and beam and column elements with concentrated plasticity. The rigid offset element was calibrated to give estimation of the initial stiffness based on the shear demand, while each of beam and column elements included two rotational springs in series which represented the nonlinear behavior of beam and column and connection [17]. The seismic response and the potential of improving the seismic performance of interior RC wide beam–narrow column joints based on ACI 318-08 and ACI-ASCE 352-02 was evaluated by Elsouiri and Harajli in 2015. The results of this study showed that the seismic performance of the specimens with improved reinforcement detailing was considerably enhanced by preventing or delaying joint shear failure, higher lateral load, deformation and energy dissipation capacities [18]. Another experimental study was conducted by Mirzabagheri et al. which evaluated the performance of RC wide and conventional beam–column roof

joints under quasi-static cyclic load. The results revealed that the strength of roof wide beam column joint was lower than the one of conventional joint. While both of them had almost equal energy dissipation capacity, the conventional joint reached its expected capacity but wide beam–column joint did not. In addition, wide beam–column joint had sufficient joint shear strength unlike the conventional one [10]. In 2017 joint shear capacity, deformation and cracking pattern of RC beam–column connections were evaluated by Najafgholipour et al. using finite element analysis [19]. The influence of beam width ratio on seismic performance of exterior RC wide beam–column connections was assessed by Behnam et al. in 2017. The ratio of beam width and joint shear stress ratio were variable parameters. The results demonstrated that joints with beam width ratios of 1 and 1.5 and shear stress ratio of 0.74 and 1.12 were capable of supporting the complete formation of beam plastic hinges with no major cracks. On the other hand, connection with beam width ratios of 2 and 2.5 and shear stress ratio of 1.63 and 2.03 showed remarkable damage at the joint core. Moreover, torsional failure of the spandrel beam was seen in the model with beam width ratio of 2.5 [20]. Behnam et al. analyzed the performance of RC wide beam–column connections. In their study various parameters including column axial load, dimensions of beam and column, the ratio of bar anchorage and reinforcement of spandrel beam were investigated numerically and experimentally using the concrete damaged plasticity (CDP) model [21].

Designing structures with high ductile behavior which undergo large deformation without losing their ability to stay in service is one of the researchers’ concerns in seismic zones [11]. In this study, the effect of column and beam dimensions on seismic behavior of RC wide column–beam joints was investigated. Hence, 27 numerical models were developed in nonlinear finite element software to analyze the influence of dimension changes on the displacement ductility and curvature ductility. After analyzing the FE outcomes, the best ratio of column and beam dimensions is discussed and equations for calculating displacement ductility and curvature ductility are suggested.

## 2 Concrete Damage Plasticity Model

The main failure mechanisms for the concrete material are cracking in tension and crushing in compression based on fundamental assumption of CDP [21–23]. The dissipated fracture energy required to generate micro cracks is investigated to define the danger in quasi-brittle materials [24]. The main assumptions of CDP model are described below:

Strain rate decomposition which is assumed for the rate-independent model is calculated using Eq. (1) [21, 23]:

$$\dot{\epsilon} = \dot{\epsilon}^{el} + \dot{\epsilon}^{pl}, \quad (1)$$

where  $\dot{\epsilon}$  is the total strain rate,  $\dot{\epsilon}^{el}$  is the elastic part of the strain rate and  $\dot{\epsilon}^{pl}$  is the plastic part of the strain rate [20, 21, 25, 26]. The relationship between strain and stress is based on Scalar damaged elasticity:

$$\sigma = (1 - d)D_0^{el} : (\epsilon - \epsilon^{pl}) = D^{el} : (\epsilon - \epsilon^{pl}), \tag{2}$$

where  $D_0^{el}$  is the initial (undamaged) elastic stiffness of the material;  $D^{el} = (1 - d)D_0^{el}$  is the degraded elastic stiffness; and  $d$  is the Scalar stiffness degradation variable which could be considered from 0 (undamaged material) to 1 (completely damaged material). Reduction in the elastic stiffness is due to concrete damage which is the result of failure mechanism of the concrete [23]. According to Scalar-damage theory, the stiffness degradation is isotropic and characterized by a single degradation parameter,  $d$ . Following the continuum damage mechanics, the effective stress is calculated by Eq. (3) [21–23]:

$$\underline{\underline{\bar{\sigma}}} \text{ def } D_0^{el} : (\epsilon - \epsilon^{pl}). \tag{3}$$

The Cauchy stress is related to the effective stress through the Scalar degradation relation [21–23]:

$$\sigma = (1 - d)\bar{\sigma}. \tag{4}$$

To consider damage states in tension and compression two hardening variables,  $\bar{\epsilon}_t^{pl}$  and  $\bar{\epsilon}_c^{pl}$ , are assigned.  $\bar{\epsilon}_t^{pl}$  which is referring to equivalent plastic strain in tension and  $\bar{\epsilon}_c^{pl}$  which is referring to equivalent plastic strain in compression [21]. When the values of the hardening parameters increase, micro cracking and propagation of cracks initiate in concrete [19,

21]. Najafgholipour et al. [19], Behnam et al. [21] and Lubliner et al. [27] proposed a model to define the yield surface function and then it was modified by (see Fig. 1) Najafgholipour et al. [19], Behnam et al. [21] and Lee and Fenves [24]. Their model considered various evolution of concrete tensile and compressive strength. The yield surface function is defined in the form of effective stress using Eq. (5):

$$F = \frac{1}{1 - \alpha}(\bar{q} - 3\alpha\bar{p} + \beta(\bar{\epsilon}^{pl})(\bar{\sigma}_{\max} - \gamma(\bar{\sigma}_{\max})) - \bar{\sigma}_c(\bar{\epsilon}_c^{pl})) \leq 0, \tag{5}$$

where  $\bar{q}$  is the equivalent von Mises stress,  $\bar{p}$  is the effective hydrostatic pressure,  $\langle x \rangle = \frac{1}{2}(x + |x|)$  is the Macauley bracket function;  $\bar{\sigma}_{\max}$  is the algebraically maximum eigenvalue of tensor  $\bar{\sigma}_c$ ;  $\alpha$ ,  $\beta$  And  $\gamma$  Are dimensionless material constant which are defined by Eqs. (6–8) [21]:

$$\alpha = \frac{(\sigma_{b0}/\sigma_{c0}) - 1}{2(\sigma_{b0}/\sigma_{c0}) - 1}; \quad 0 \leq \alpha \leq 0.5, \tag{6}$$

where  $(\sigma_{b0}/\sigma_{c0})$  is the ratio of biaxial compressive to uniaxial compressive yield stress which affects the yield surface in a plane stress state. Typical value of the ratio  $(\sigma_{b0}/\sigma_{c0})$  for concrete based on experimental results is in the range from 1.10 to 1.16. Consequently, the values of  $\alpha$  will be between 0.08 and 0.12:

$$\beta(\bar{\epsilon}^{pl}) = \frac{\bar{\sigma}_c(\bar{\epsilon}_c^{pl})}{\bar{\sigma}_t(\bar{\epsilon}_t^{pl})}(1 - \alpha) - (1 + \alpha), \tag{7}$$

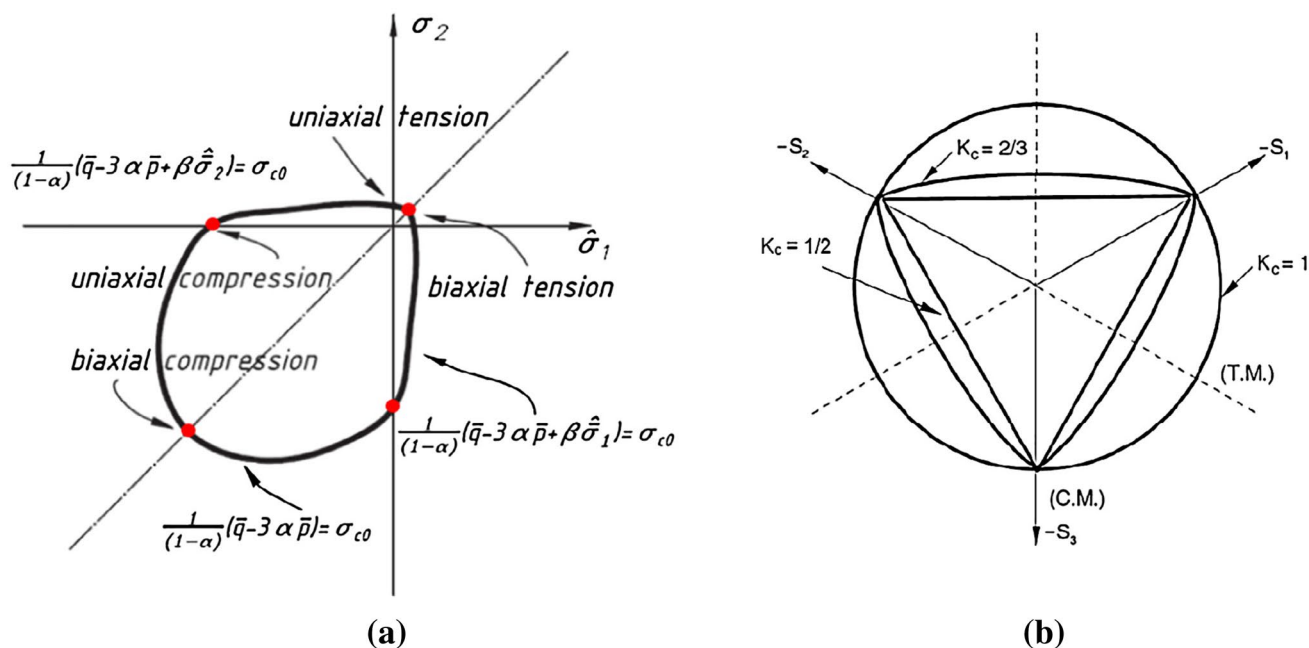


Fig. 1 Concrete damage plasticity model [24]: a yield surface in plane stress and b yield surface in the deviatoric plane [21]

where  $\bar{\sigma}_c(\bar{\epsilon}_c^{pl})$  and  $\bar{\sigma}_t(\bar{\epsilon}_t^{pl})$  are the effective cohesion stress in compression and tension, respectively:

$$\gamma = \frac{3(1 - k_c)}{2k_c - 1} \tag{8}$$

The  $\gamma$  coefficient appears only for triaxial compression stress state and can be determined by comparing the yield condition along the tensile and compressive meridians. The parameter  $k_c$  is the ratio of the hydrostatic effective stress in tensile meridian to that one the compressive meridian when the maximum principal stress is negative. This parameter is the coefficient ascertain the shape of the deviatoric cross section, as shown in Fig. 1. The shape of deviatoric plane was first assumed to be circular as in the classic Drucker-Prager strength hypothesis ( $k_c = 1$ ). The CDP damage suggests to assume default value of  $k_c = 2/3$  based on triaxial stress test results.

The flow rule is used to connect the yield surface stress and the concrete stress–strain relationship. The CDP model uses Drucker-Prager hyperbolic function as non-associated flow potential function using Eq. (9):

$$G = \sqrt{(\zeta \sigma_{t0} \tan \psi)^2 + \bar{q}^2} - \bar{p} \tan \psi, \tag{9}$$

where  $\zeta$  is the potential flow eccentricity which adjusts the shape of hyperbola in the plastic potential flow function.  $\zeta$  is a small positive value which can be estimated as the ratio of concrete tensile strength to its compressive strength,  $\sigma_{t0}$  is the uniaxial tensile stress.  $\psi$  is the dilation angle which is a concrete performance characterizing parameter when it is subjected to triaxial compound stress state.

Static analysis in ABAQUS with viscosity regularization was performed. A full Newton solver with default matrix storage was used to solve this numerical model by ABAQUS. Newton–Raphson equilibrium iteration provides convergence at the end of each load increment within tolerance limits for all degree of freedoms in the model [19, 21]. An automatic incremental is used to analyze this model by ABAQUS. A small time step size and a large maximum number of increments were defined to enhance the coverage rate.

### 3 Numerical Models

To evaluate seismic behavior of RC wide column–beam joints, force–displacement and moment–curvature diagrams were considered and investigated. 27 numerical models, therefore, were analyzed in FEM software, ABAQUS.

### 3.1 Methodology

To generate concrete beam and column the 8-noded brick element (C3D8R) with reduced integration and three degrees of freedom in every node was used. The element used to model steel reinforcement bars is the two-noded truss element (T3D2) with three degrees of freedom in every node. To simulate the concrete-reinforcement reaction embedded method with perfect bond between concrete and steel was adopted which allows for approximate bond stress–slip constitutive model and transfer force from concrete to reinforcement bars across cracks [19, 21]. To consider the concrete-steel interaction after cracking (such as bond slip and dowel action) a simplified way using tension stiffening in the concrete model was adopted [19, 21, 25].

### 3.2 Concrete

#### 3.2.1 Compressive Behavior of Concrete

As demonstrated in Fig. 2, the stress–strain behavior of concrete was simulated using Eqs. (10a–10c) [29, 30]:

$$\sigma_{c,1} = E_c \epsilon_c, \quad \epsilon_c \leq \frac{0.4f'_c}{E_c}, \tag{10a}$$

$$\sigma_{c,2} = \frac{\eta_c \frac{\epsilon_c}{\epsilon_0} - \left(\frac{\epsilon_c}{\epsilon_0}\right)^2}{1 + (\eta_c - 2) \frac{\epsilon_c}{\epsilon_0}} f'_c, \quad \frac{0.4f'_c}{E_c} \leq \epsilon_c \leq 0.0035, \tag{10b}$$

$$\sigma_{c,3} = \left( \frac{2 + \lambda_c f'_c \epsilon_0}{2f'_c} - \lambda_c \epsilon_0 + \frac{\lambda_c \epsilon_c^2}{2\epsilon_0} \right)^{-1}, \quad 0.0035 \leq \epsilon_c \leq 0.03. \tag{10c}$$

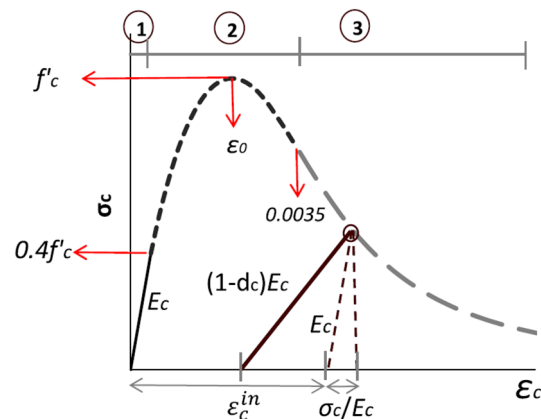


Fig. 2 Uniaxial compressive stress–strain relationship for concrete [20]

Equation (10a) represents the linear elastic branch in which  $\epsilon_c$  is a variable changing from zero to  $0.4f'_c/E_c$ , and  $E_c$  is the initial modulus of elasticity. The linear branch ends at the stress level of  $0.4f'_c$ . Equation (9) describes the second branch up to the strain level of 0.0035 in the descending branch. The corresponding strain level at the peak stress is defined as  $\epsilon_0 = 2f'_c/E_c$ ;  $\eta_c$  is the material constant. The stress and strain compatibility at the strain level of  $\epsilon_c = 0.4f'_c/E_c$ , for Eqs. (10a) and (10b) gives the value of  $\eta_c$ . Eq. (10c) shows the third and descending branch;  $\lambda_c$  is the constant crushing energy as a material property [30]. Using the stress and strain compatibility at the strain level of  $\epsilon_c = 0.0035$ , for Eqs. (10b) and (10c) enables the value of  $k_c$  to be determined. The concrete ultimate strain  $\epsilon_u$  was set to a large value of 0.035 to avoid any numerical difficulties [21, 29].

The other CDP input parameters, which were considered in this study to complete the yield surface and the non-associated potential flow, are provided in Table 1.

### 3.2.2 Tensile Behavior of Concrete

Linear uniaxial stress–strain behavior of concrete is one of the assumptions in this study which is assigned in the FEA. Based on this assumption, tensile behavior of concrete consists of two stages. In the first stage, concrete has a linear elastic behavior before reaching the concrete tensile strength,  $\sigma_{t0}$ . The second stage starts together with crack occurrence and its propagation in concrete under tension. The linear, bilinear or nonlinear model of Belbarbi and Hsu [31] was used to model softening procedure of concrete material, as illustrated in Fig. 3.

Equation (11) which is suggested by Genikomsou and Polak [32] and Wang and Vecchio [33] was used to estimate the tensile strength of concrete:

$$f'_t = 0.33\sqrt{f'_c}. \tag{11}$$

In CDP model, the damage due to both uniaxial tension and compression during softening procedure is considered and is defined in FE analysis. Damage in comparison occurs when the concrete stress reaches the stress corresponding to strain level  $\epsilon_0$  which is the maximum uniaxial compressive strength [19].

**Table 1** CDP input parameters

Parameter	$\sigma_{b0}/\sigma_{c0}$	$k_c$	$\psi$	$\xi$	$\mu$ (s)
Value	1.16	0.667	40°	0.1	0.00001

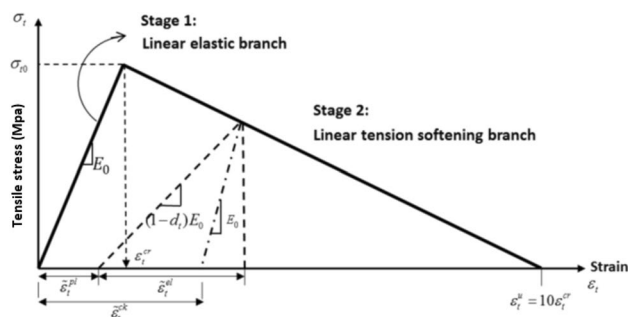


**Fig. 3** Uniaxial tensile stress–strain behavior for concrete and its softening branch assumptions [20]

### 3.3 Steel

The uniaxial tensile stress–strain behavior of reinforcement was assumed to be elastic with conventional Young’s modulus and Poisson’s ratio. The plastic behavior is also modeled including yield stress and corresponding plastic strain. Properties of plastic phase is defined to the model using bilinear behavior. The typical stress–strain behavior of reinforcement bars is demonstrated in Fig. 4 [19].

### 3.4 Details of Models

Totally 27 RC wide column–beam joints were modeled in ABAQUS. Three of them were modeled to be verified by similar experimental ones studied by Li et al. (C1A, C1B and E1B) the other ones were made by changing dimensions of the model C1A. The height and width of columns and beams of models are presented in Table 2.

Twelve 20 mm diameter bars were considered for longitudinal reinforcement in columns and 8 mm diameter bars at 150 mm provided transverse reinforcement for both the beams and columns, as shown in Fig. 5b–d (Table 3). Longitudinal reinforcement of beams varies and the details are presented in Table 4.

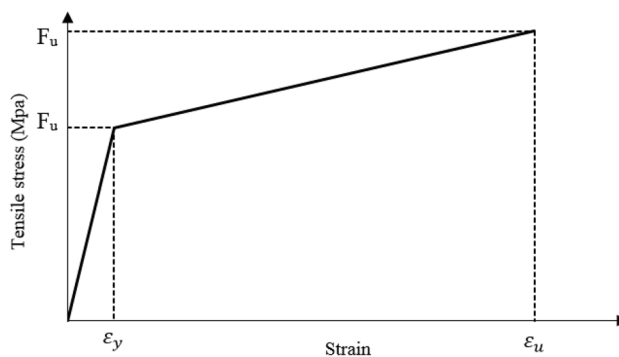


**Fig. 4** Uniaxial stress–strain behavior of reinforcements bars



**Table 2** Dimensions of numerical models

Names of models	Column		Beam	
	$C_w$	$C_h$	$B_w$	$B_h$
	Width (mm)	Height (mm)	Width (mm)	Height (mm)
1	820	280	230	650
2	820	280	250	600
3	820	280	300	500
4	820	280	375	400
5	820	280	400	375
6	820	280	500	300
7	750	300	230	650
8	750	300	250	600
9	750	300	300	500
10	750	300	375	400
11	750	300	400	375
12	750	300	500	300
13	620	370	230	650
14	620	370	250	600
15	620	370	300	500
16	620	370	375	400
17	620	370	400	375
18	620	370	500	300
19	500	460	230	650
20	500	460	250	600
21	500	460	300	500
22	500	460	375	400
23	500	460	400	375
24	500	460	500	300

### 3.5 Boundary Conditions and Loading

Boundary conditions, which are illustrated in Fig. 5a, were assigned to the numerical models the same as experimental specimens; Pinned joint was considered for the bottom of the columns. The end of the beams was modeled roller; in other words, just the vertical degree of freedom was restrained. Loading was determined in two steps. First, an axial load of  $0.1A_g f'_c$  was applied on top surface of the column, and then, the horizontal displacement shown in Fig. 6 was applied in X-direction on top of the column. The analysis was continued to the same displacement as the test (133 mm) [14, 15].

### 3.6 Material Properties

The Young's Modulus and Poissons's Ratio of concrete were considered 20,302 Mpa and 0.15, respectively. The yield strength,  $f_y$ , and the ultimate strength,  $f_u$ , for reinforcement bars number 8 were considered 510 N/mm<sup>2</sup>, 612 MPa, while they were considered 513 N/mm<sup>2</sup> and 613 MPa for reinforcement bars number 20, respectively. The yield strain,  $\epsilon_y$ , and ultimate

strain,  $\epsilon_u$ , of reinforcement bars were chosen 0.00263 and 0.09, respectively. The uniaxial tensile stress–strain behavior of reinforcement bars was assumed to be elastic with Young's Modulus and Poissons's ratio of 206,000 MPa and 0.3, respectively [14, 15]. The plastic behavior is also modeled including yield stress and corresponding plastic strain (Fig. 4).

## 4 Model Validation

Numerical RC wide column–beam joints were modeled in FEM software (Fig. 7) and were verified using the experimental study of Li et al. [14, 15]. The characteristics of numerical models such as material properties, boundary conditions, etc. were exactly the same as the experimental models. Dimensions of beam and column in all of the three connections were 230×300 and 280×820, respectively. The details of three experimental specimens used for verifying numerical models are provided in Table 5. Force–displacement diagram for the top surface of the column was considered for verifying. The size of mesh in FE Analysis can affect the results considerably. In this study, the mesh size effect is investigated by considering three sizes of 60 mm, 65 mm and 70 mm. The force–displacement diagrams of the numerical models and envelope curve of force–displacement hysteresis diagram in experimental studies are shown in Fig. 8. As it could be seen in Fig. 8, the mesh size of 65 mm leads to more reliable results in comparison to the other ones; therefore, the mesh size of other models is considered 65 mm.

## 5 Analytically Results

As mentioned before, the novel objective of this research is to find the relation between the beam and column dimensions and seismic behavior of RC wide column–beam joints; consequently, two main seismic parameters are presented and discussed: displacement ductility and curvature ductility.

### 5.1 Displacement Ductility

Force–displacement diagrams of 24 numerical models are shown in Fig. 9.

Displacement ductility,  $\mu_\Delta$ , is defined as the ratio of ultimate displacement,  $\Delta_u$ , to yield displacement,  $\Delta_y$  (Eq. 12) [34]:

$$\mu_\Delta = \frac{\Delta_u}{\Delta_y} \quad (12)$$

Ultimate displacement,  $\Delta_u$ , is defined as the displacement corresponding to 15% drop of loading capacity. There are two different methods for obtaining yield displacement; the balance of energy is used to find yield displacement in the

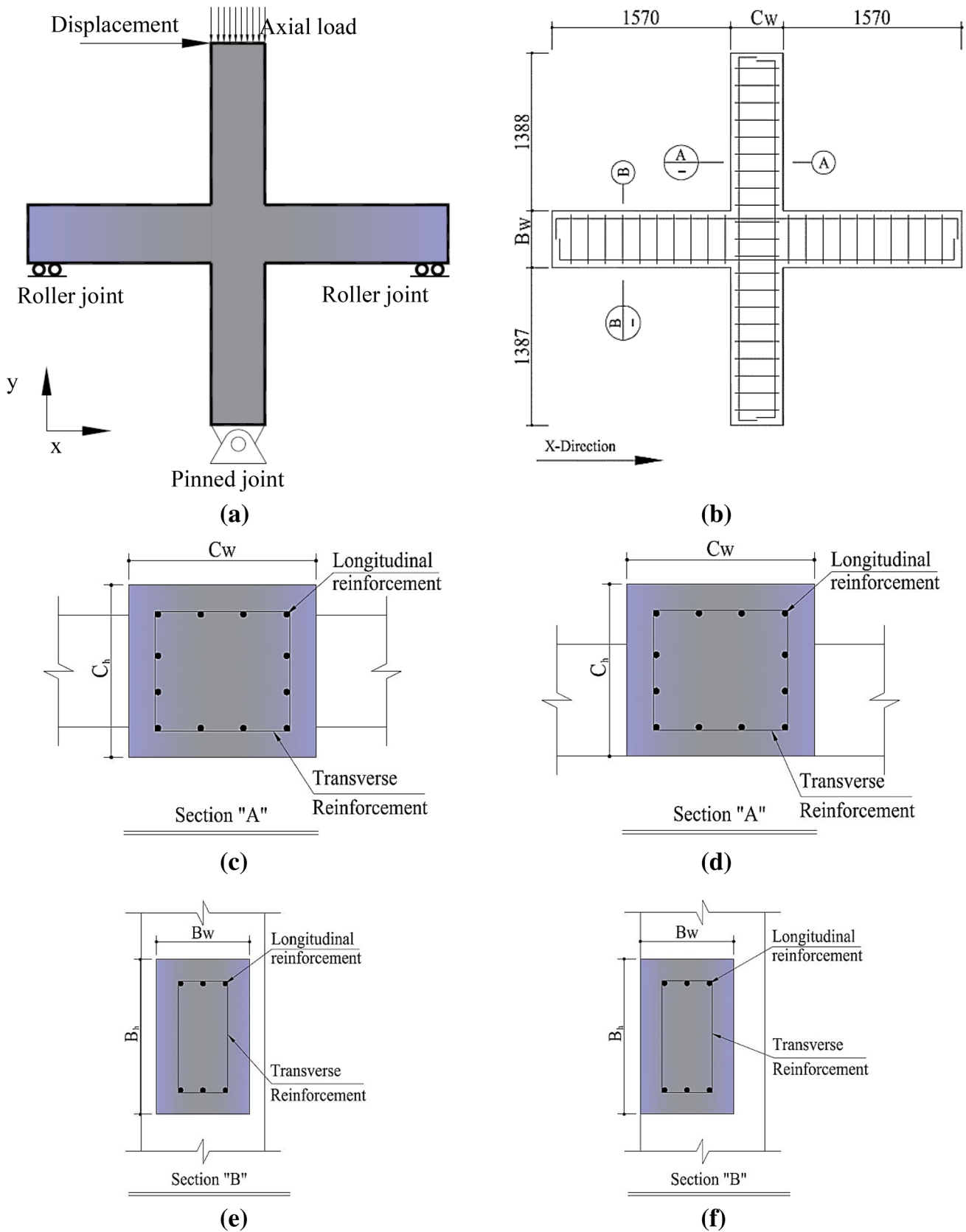


**Fig. 5** a Boundary conditions of models, b reinforcement of models, c Section "A" for C1A, C1B, d Section "A" for E1B, e Section "B" for C1A, C1B, f Section "B" for E1B

**Table 3** Details of column reinforcement

Section of columns	Detail of reinforcement	
	Longitudinal reinforcement	Transverse reinforcement
$C_w820C_h280$	$12\bar{\Phi}20$	$\Phi8@150\text{ mm}$
$C_w750C_h300$	$12\bar{\Phi}20$	$\Phi8@150\text{ mm}$
$C_w620C_h370$	$12\bar{\Phi}20$	$\Phi8@150\text{ mm}$
$C_w500C_h460$	$12\bar{\Phi}20$	$\Phi8@150\text{ mm}$

**Table 4** Details of beam reinforcement

Section of beams	Detail of reinforcement		
	Longitudinal reinforcement		Transverse reinforcement
	Bottom layer	Top layer	
$B_w230B_h650$	$3\bar{\Phi}20$	$3\bar{\Phi}20$	$\Phi8@150\text{ mm}$
$B_w250B_h600$	$3\bar{\Phi}20$	$3\bar{\Phi}20$	$\Phi8@150\text{ mm}$
$B_w300B_h500$	$3\bar{\Phi}20$	$3\bar{\Phi}20$	$\Phi8@150\text{ mm}$
$B_w375B_h400$	$3\bar{\Phi}20$	$3\bar{\Phi}20$	$\Phi8@150\text{ mm}$
$B_w400B_h375$	$3\bar{\Phi}20$	$3\bar{\Phi}20$	$\Phi8@150\text{ mm}$
$B_w500B_h300$	$5\bar{\Phi}16$	$5\bar{\Phi}20$	$\Phi8@150\text{ mm}$

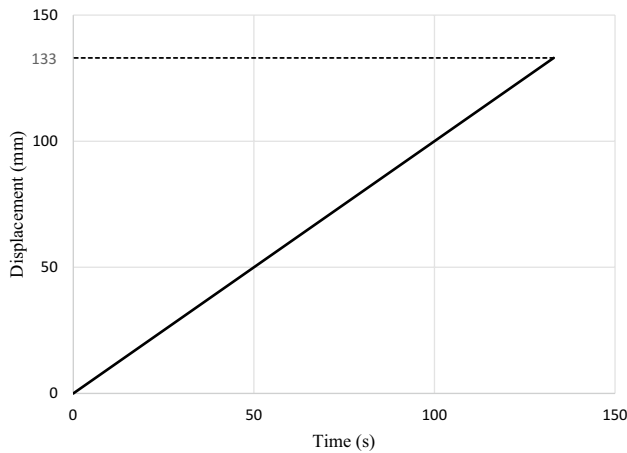


**Fig. 6** Diagram of displacement–time history applied on top of the column in all of the numerical models

first method. As shown in Fig. 10a [4], a secant line passing the origin point  $O$  and a point  $I$  on the curve intersects the peak strength at point  $A$ . The secant line should be adjusted in a way that area  $A_1$  equals to area  $A_2$ ; the displacement corresponding to the secant line (point  $A$ ) is considered as the yield displacement.

In the other method, which is based on general yielding, a line for elastic behavior intersects the peak strength at point

$H$ , as illustrated in Fig. 10b. The vertical line passing point  $H$  intersects the load–displacement curve at point  $I$ . The secant line passing point  $O$  and point  $I$  intersects strength at point  $A$  which is defined as the yield displacement [4]. In this study the first method is used to obtain yield displacement.

Displacement ductility of all of the 24 models calculated using above-mentioned equation are presented in Table 5. Based on Table 6, the maximum displacement ductility belongs to the model 24 ( $C_w/B_w = 1$ ) with the size of 4.54. On the other hand, model 9 ( $C_w/B_w = 2.50$ ) has the minimum displacement ductility with the size of 1.22.

### 5.2 Curvature Ductility

Moment–curvature diagram of numerical RC wide column–beam joints are illustrated in Fig. 11. It should be noted that both curvature and moment are calculated at the beam section, where the beam meets the column.

Equation 13 is used to calculate curvature ductility [34]. According to this equation, curvature ductility is the ratio of ultimate curvature to yield curvature:

$$\mu_\phi = \frac{\phi_u}{\phi_y}, \tag{13}$$

where  $\phi_u$  is the curvature at ultimate when the concrete compression strain reaches a specified limiting value,  $\phi_y$  is the curvature when the tension reinforcement first reaches the yield strength. The definition of  $\phi_y$  shows the influence of the yield strength of reinforcement bars on the calculation of  $\mu_\phi$ , while the definition of  $\phi_u$  reflects the effect of ultimate strain of concrete in compression. The yield curvature of a RC section is taken when the tension steel reaches the yield stress (Fig. 12a) and is calculated using Eq. (14) [34]:

$$\phi_y = \frac{\epsilon_{sy}}{(1-k)d} = \frac{f_y}{E_s(1-k)d}. \tag{14}$$

The parameter  $k$  is calculated using Eq. (15):

$$k = \left( (\rho + \rho')^2 n^2 + 2 \left( \rho + \frac{\rho' d'}{d} \right) n \right)^{0.5} - (\rho + \rho') n, \tag{15}$$

where  $A_s$  is the area of tension steel bars,  $A'_s$  is the area of compression steel bars,  $b$  is the width of section,  $d$  is the effective depth of tension steel,  $d'$  is the distance from extreme compression fiber to centroid of compression steel bars,  $E_c$  is the modulus of elasticity of concrete,  $E_s$  is the modulus of elasticity of steel,  $f_y$  is the yield strength of steel,  $n$  is the ratio of  $E_s$  to  $E_c$ ,  $\rho = A_s/bd$  and  $\rho' = A'_s/bd$ .

The ultimate curvature of a RC section is defined as the maximum value of concrete strain at the extreme compression fiber (Fig. 12b) and is calculated using Eq. (16):



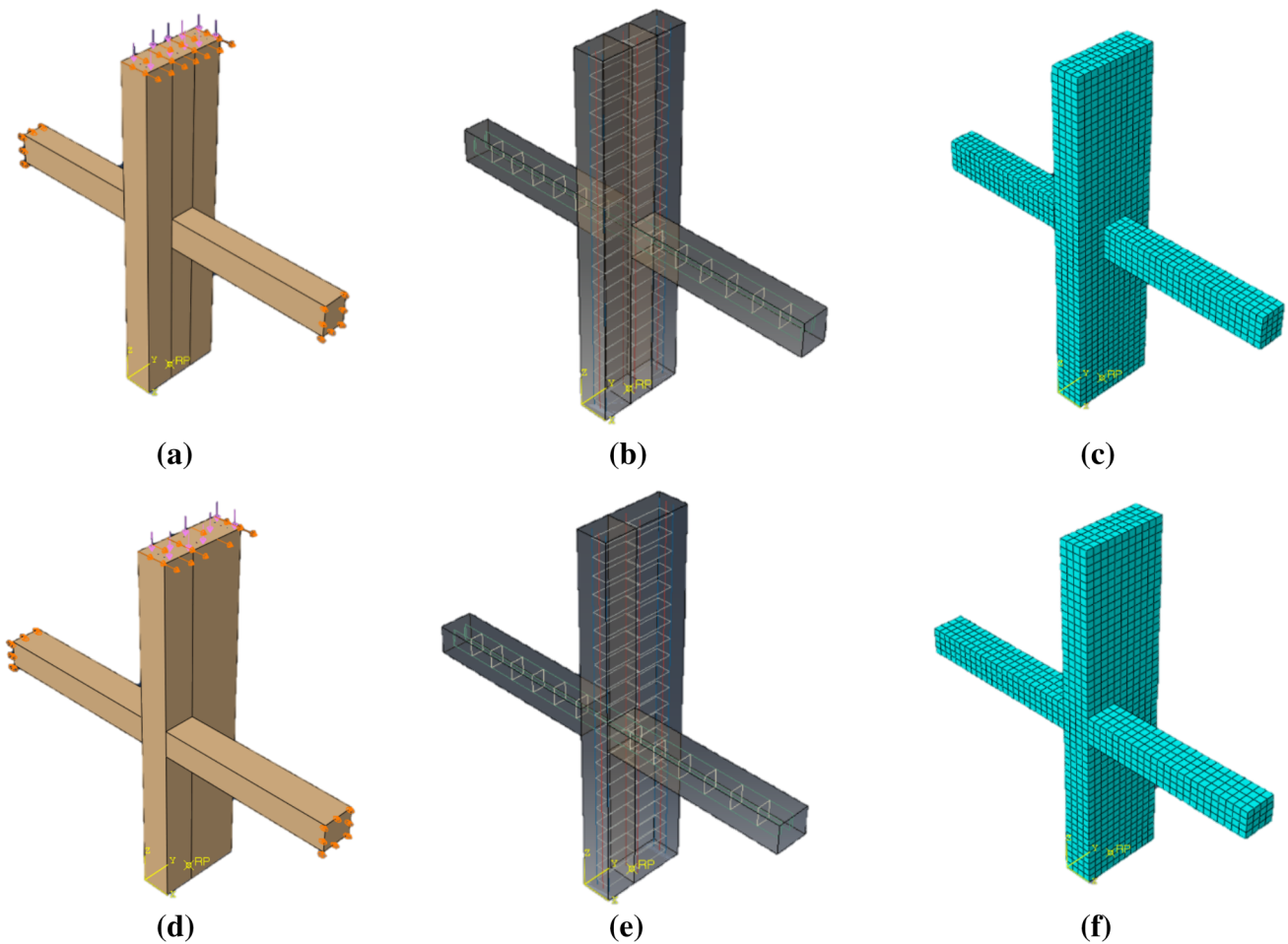


**Fig. 7** **a** Defined boundary condition in FEM software for C1A and C1B, **b** reinforcement geometry for C1A and C1B, **c** model geometry and mesh for C1A and C1B, **d** defined boundary condition in FEM software for E1B, **e** reinforcement geometry for E1B, **f** model geometry and mesh for E1B

**Table 5** Details of experimental specimens

Name of experimental specimens	Beam		Column		$f'_c$ (MPa)	Axial load	Joint type
	Longitudinal reinforcement	Transverse reinforcement	Longitudinal reinforcement	Transverse reinforcement			
C1A	Top: 2 $\Phi$ 13 Bot.: 2 $\Phi$ 13	$\Phi$ 10@230	8 $\Phi$ 25	$\Phi$ 10@125	19.2	$0.1A_g f'_c$	Concentric
C1B	Top: 2 $\Phi$ 13 Bot.: 2 $\Phi$ 13	$\Phi$ 10@230	8 $\Phi$ 25	$\Phi$ 10@125	19.0	$0.35A_g f'_c$	Concentric
E1B	Top: 2 $\Phi$ 13 Bot.: 2 $\Phi$ 13	$\Phi$ 10@230	8 $\Phi$ 25	$\Phi$ 10@125	18.4	$0.35A_g f'_c$	Eccentric

$$\phi_u = \frac{\epsilon_c}{c} \tag{16}$$

The value of  $\epsilon_c$  is considered 0.004 [33]. Table 7 provides the data relating to the curvature ductility of 24 numerical wide column–beam joints. Based on this

table, the maximum and minimum sizes of curvature ductility belong to model 24 ( $C_w/B_w = 1.00$ ) and model 1 ( $C_w/B_w = 3.57$ ), respectively.

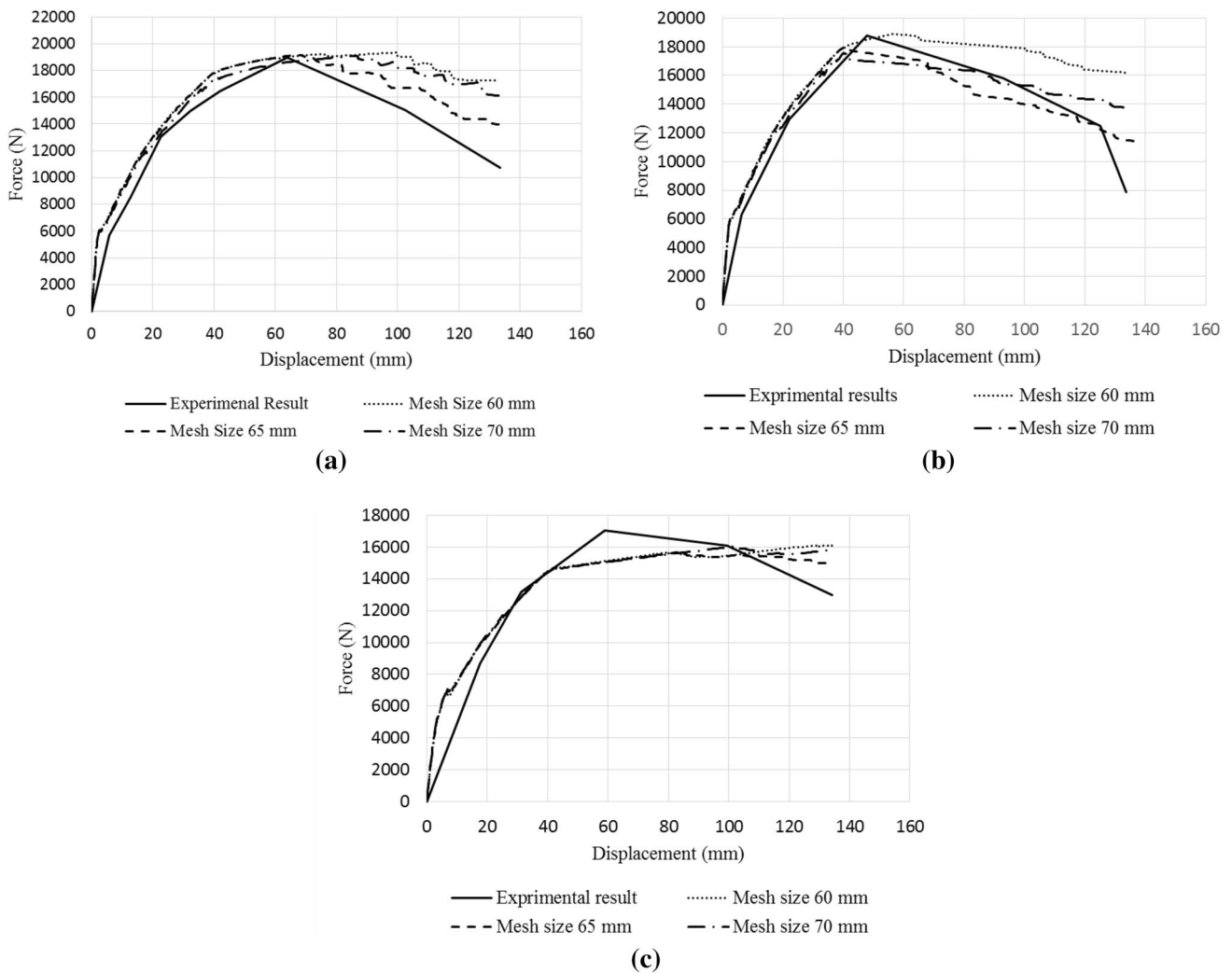


Fig. 8 Force–displacement diagram of numerical and experimental models: a C1A, b C1B, c E1B

## 6 Estimation of Seismic Response of Joint

### 6.1 Displacement Ductility

By changing the dimensions of beams and columns, displacement ductility fluctuates; to find the relation between the dimensions of joint elements and displacement ductility, however, the values of displacement ductility of all the models are shown in Fig. 13 and Eq. (17) is obtained using logarithmic regression:

$$\mu_{\Delta} = -2.06 \ln \left( \frac{W_c}{W_b} \right) + 3.8236, \quad (17)$$

where  $W_c$  is column width and  $W_b$  is beam width. It should be taken into account that the difference between  $\mu_{\Delta}$  calculated by Eq. (17) and  $\mu_{\Delta}$  obtained from FE analysis for the most of the models are less than 10%.

### 6.2 Curvature Ductility

To find the equation for estimating curvature ductility, the FEA outcomes for all of the models are demonstrated in Fig. 14. Consequently, Eq. (18) is obtained using power regression and is suggested for estimating curvature ductility:

$$\mu_{\psi} = 11.467 \left( \frac{C_w}{B_w} \right)^{-1.683}, \quad (18)$$

where  $C_w$  is column width and  $B_w$  is beam width. It should be mentioned that both Eqs. (17) and (18) are suggested for joints with the  $A_s$  used in this study and cannot be used for all joints.

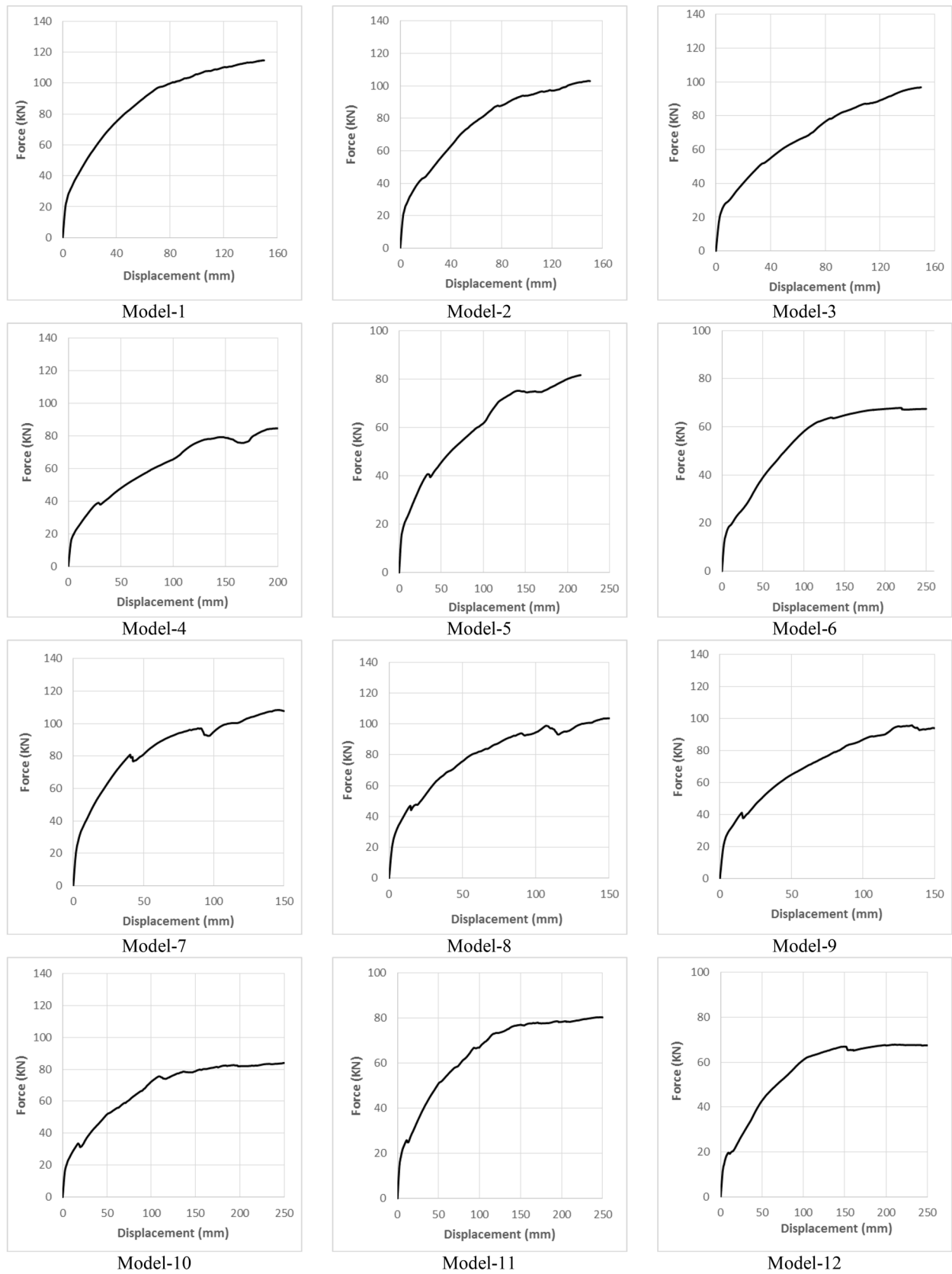


Fig. 9 Force–displacement diagram of numerical models

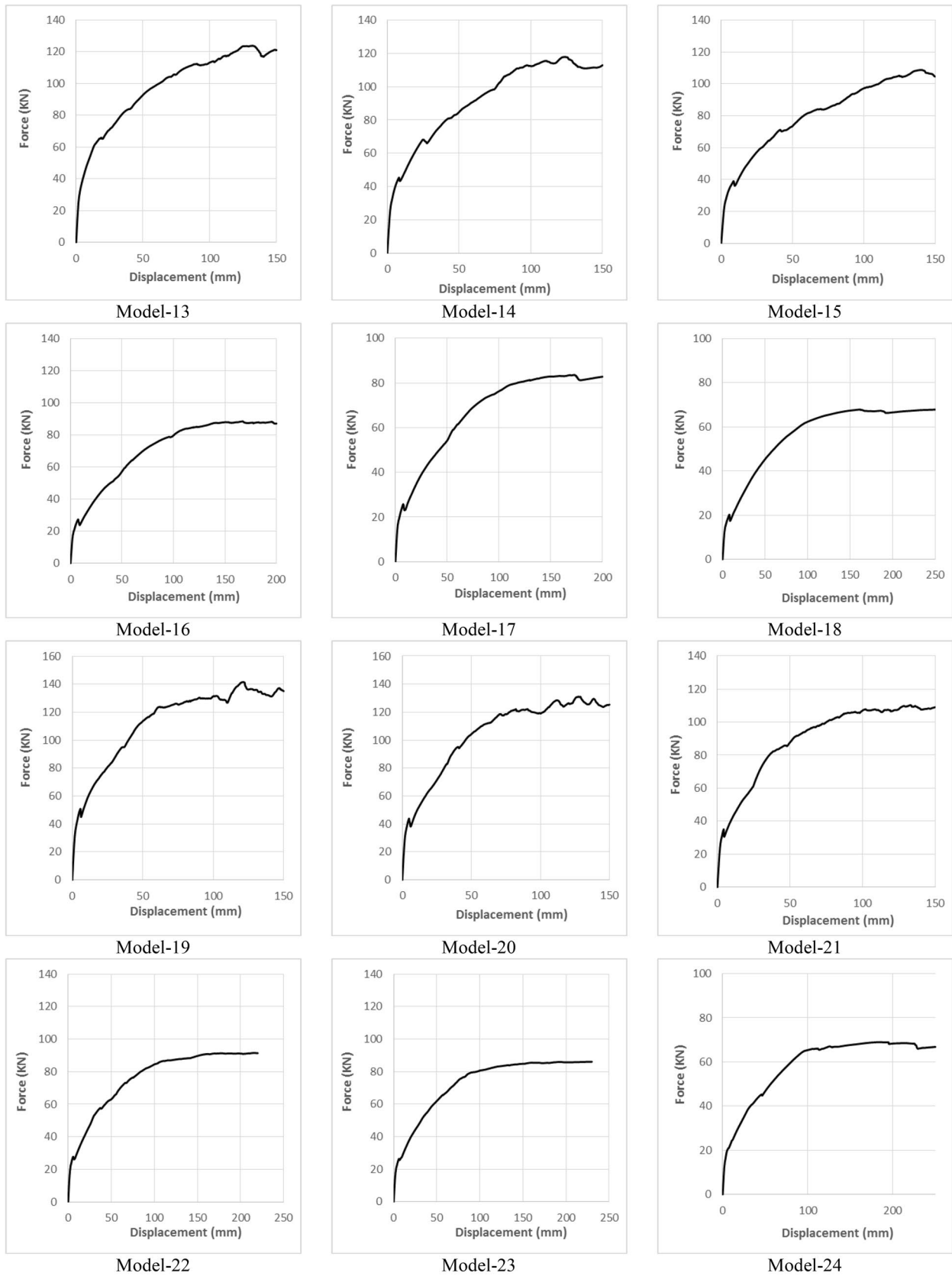
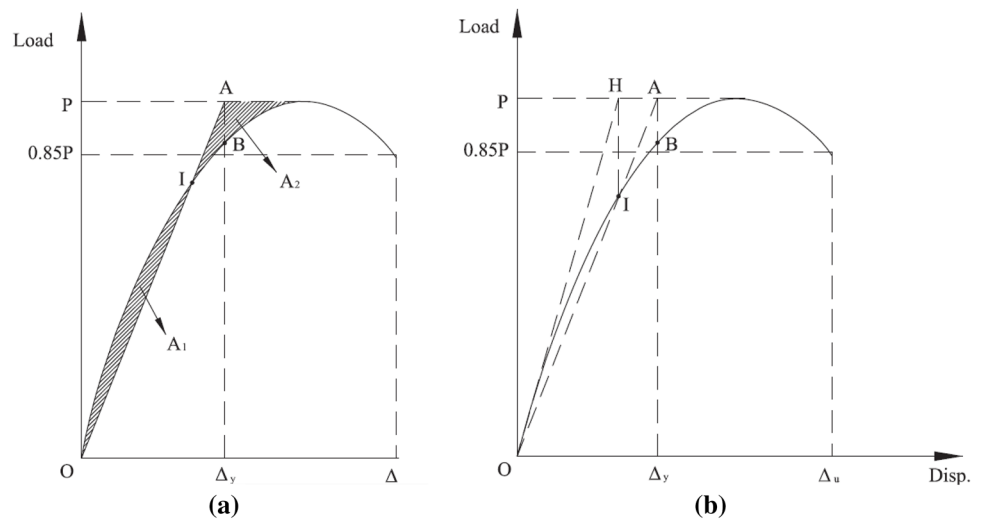


Fig. 9 (continued)

**Fig. 10** Yield displacement definitions: **a** energy balance method, **b** general yielding method [4]



### 7 Discussions

The main objective of this study is to investigate the effect of beam and column dimensions on the seismic response of RC wide column–beam joints. To achieve the goal, four different parameters including the ratio of  $C_w/B_w$ ,  $C_w/C_h$ ,  $B_w/B_h$  and  $\rho_{col}$  are changed in numerical models and the results are discussed.

#### 7.1 The Effect of $C_w/B_w$ on Displacement Ductility and Curvature Ductility

To evaluate the effect of  $C_w/B_w$  on the seismic response of the joints, they are classified in six groups and in each of which column dimensions were changed, while beam dimensions remained constant. Based on the numerical results, by decreasing the ratio of  $C_w/B_w$ , the curvature ductility increases, while displacement ductility fluctuates. In other words, although in the models with  $B_w/B_h \geq 0.6$  displacement ductility increases, in the models with  $B_w/B_h \leq 0.42$  displacement ductility decreases. The proportions of the changes in displacement ductility and curvature ductility are presented below:

When the ratio of  $C_w/B_w$  decreases by 8.5%, 24.39% and 39.02%:

- In the models with  $B_w/B_h = 0.35$  displacement ductility changes by  $-5.2\%$ ,  $-22.5\%$  and  $21.23\%$ , respectively, and curvature ductility increases by  $11.61\%$ ,  $4.91\%$  and  $-32.27\%$ , respectively.
- In the models with  $B_w/B_h = 0.42$ , displacement ductility changes by  $-6.99\%$ ,  $-7.95\%$  and  $54.64\%$ , respectively, and curvature ductility changes by  $-16.26\%$ ,  $7.21\%$  and  $48.41\%$ , respectively.
- In the models with  $B_w/B_h = 0.6$ , displacement ductility changes by  $-1.24\%$ ,  $154.68\%$  and  $134.48\%$ , respectively,

**Table 6** Displacement ductility of all the numerical models

Name of models	$C_w/B_w$	Yield displacement (mm) $\Delta_y$	Ultimate displacement (mm) $\Delta_u$	Displacement ductility
1	3.57	46.76	75.04	1.60
2	3.28	54.01	102.74	1.90
3	2.73	66.71	82.32	1.23
4	2.19	100.50	173.18	1.72
5	2.05	100.43	174.75	1.74
6	1.64	90.73	209.00	2.30
7	3.26	42.47	64.57	1.52
8	3.00	47.49	84.02	1.77
9	2.50	73.85	90.00	1.22
10	2.00	60.72	177.52	2.92
11	1.88	59.15	179.83	3.04
12	1.50	81.63	207.28	2.54
13	2.70	46.93	58.36	1.24
14	2.48	42.06	73.65	1.75
15	2.07	38.00	119.43	3.14
16	1.65	56.52	184.55	3.27
17	1.55	58.79	178.76	3.04
18	1.24	78.98	230.93	2.92
19	2.17	35.64	69.34	1.95
20	2.00	28.90	85.02	2.94
21	1.67	38.04	110.08	2.89
22	1.33	55.08	175.72	3.19
23	1.25	57.73	175.72	3.04
24	1.00	50.84	230.93	4.54



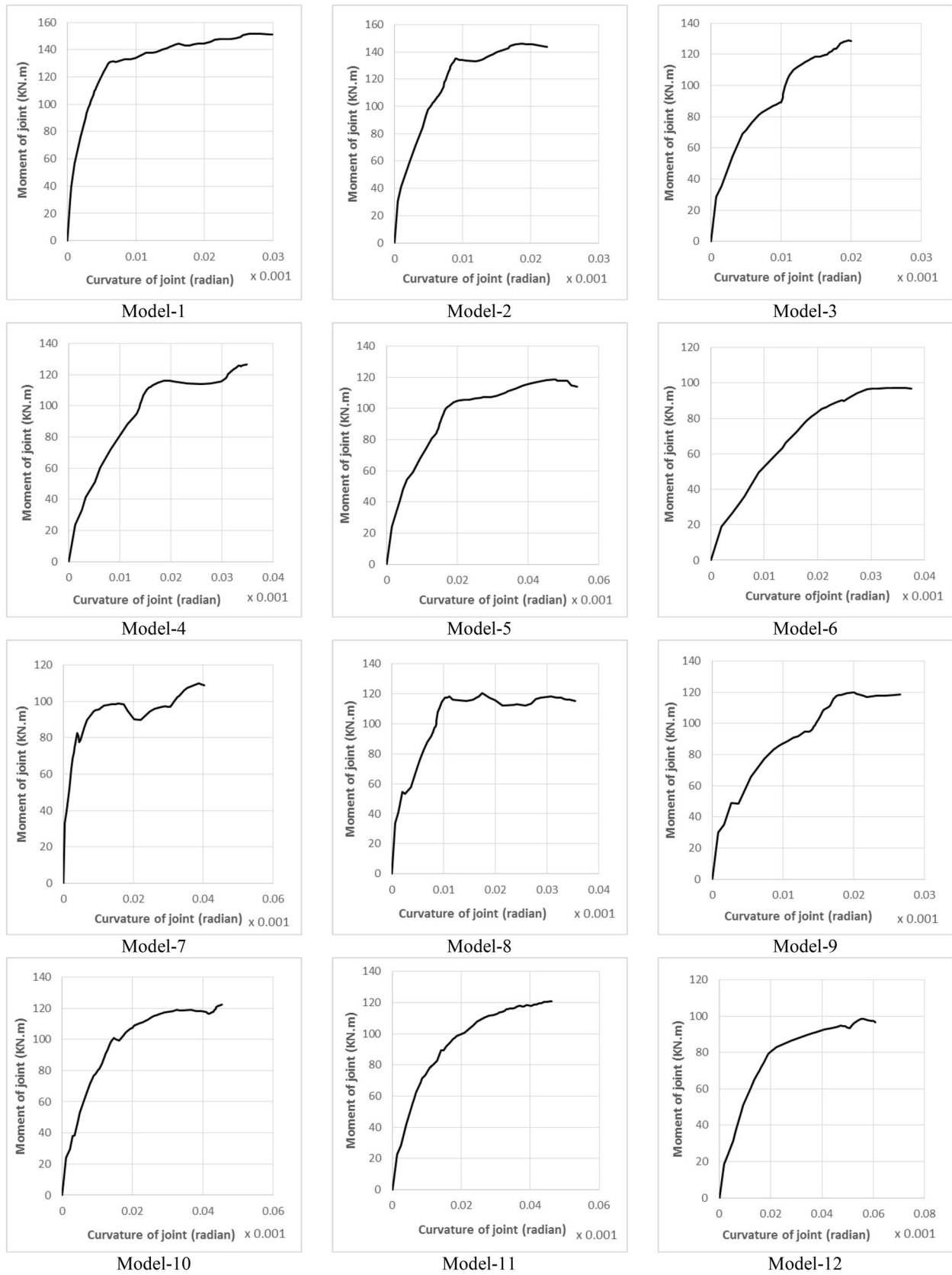


Fig. 11 Moment–curvature diagrams of numerical models

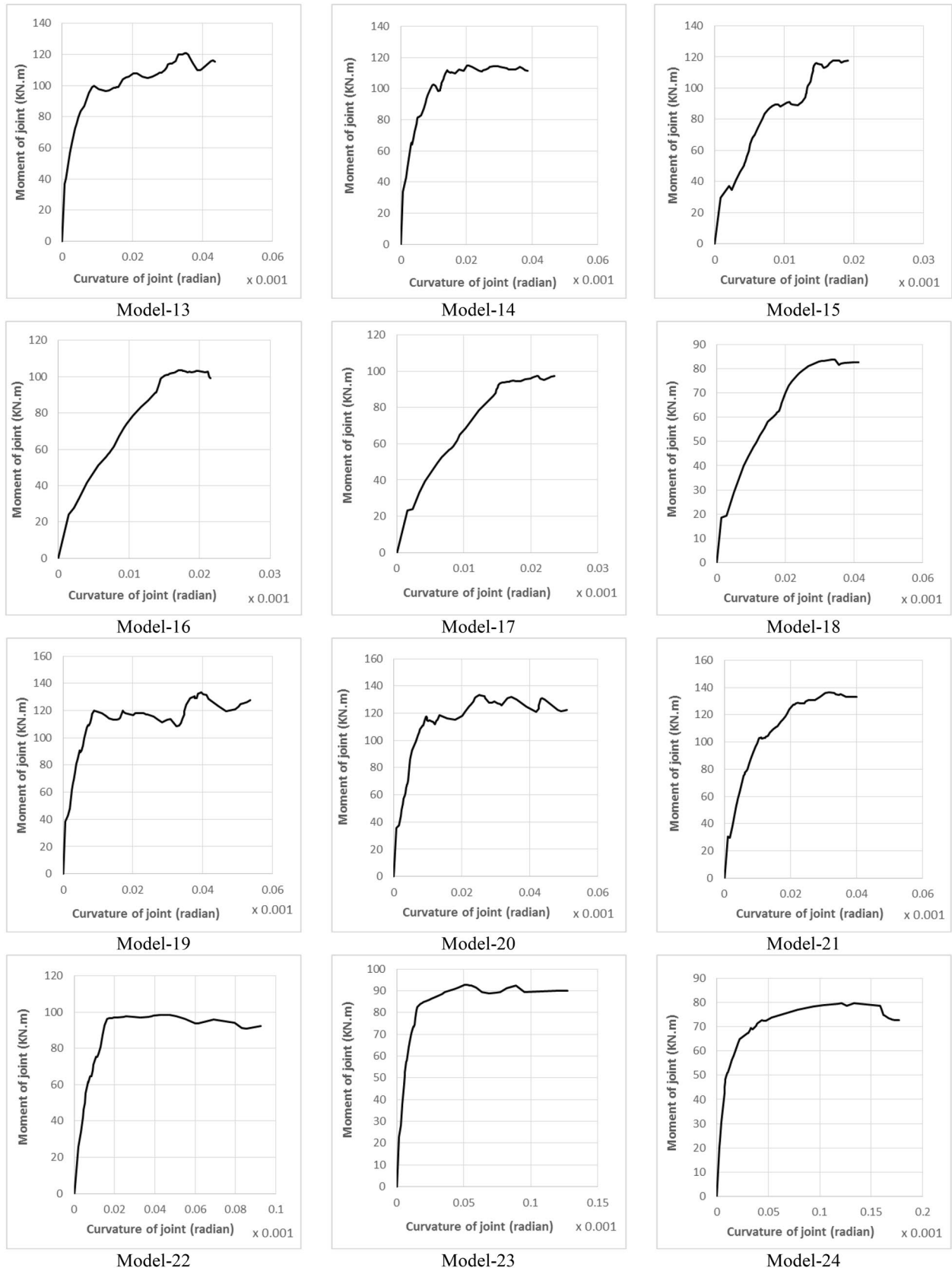
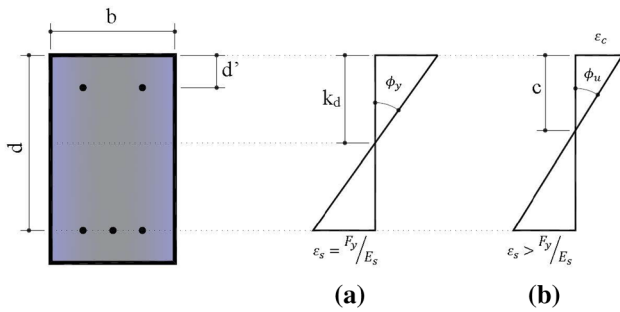


Fig. 11 (continued)



**Fig. 12** Doubly reinforced section with flexure **a** at first yield **b** at ultimate yield [35]

**Table 7** Curvature ductility of all of the numerical models

Names of models	$C_w/B_w$	Yield curva-	Ultimate curva-	Curvature ductility
		ture ( $\text{mm}^{-1}$ ) $\phi_y$	ture ( $\text{mm}^{-1}$ ) $\phi_u$	
1	3.57	5.22E-06	8.29E-06	1.59
2	3.28	6.19E-06	1.19E-05	1.92
3	2.73	7.09E-06	1.49E-05	2.10
4	2.19	6.28E-06	3.07E-05	4.90
5	2.05	6.62E-06	3.11E-05	4.70
6	1.64	8.19E-06	3.56E-05	4.34
7	3.26	4.88E-06	8.65E-06	1.77
8	3.00	6.91E-06	1.11E-05	1.61
9	2.50	5.81E-06	1.64E-05	2.83
10	2.00	7.27E-06	3.15E-05	4.34
11	1.88	7.05E-06	3.35E-05	4.74
12	1.50	8.16E-06	5.60E-05	6.86
13	2.70	5.46E-06	9.10E-06	1.67
14	2.48	4.86E-06	1.00E-05	2.06
15	2.07	5.45E-06	1.47E-05	2.70
16	1.65	6.19E-06	1.93E-05	3.12
17	1.55	6.37E-06	2.20E-05	3.45
18	1.24	7.97E-06	3.99E-05	5.00
19	2.17	4.75E-06	9.98E-06	2.10
20	2.00	4.24E-06	1.21E-05	2.85
21	1.67	4.93E-06	2.30E-05	4.66
22	1.33	5.71E-06	6.16E-05	10.79
23	1.25	6.15E-06	5.60E-05	9.09
24	1.00	9.04E-06	1.60E-04	17.69

and curvature ductility increases by 34.86%, 28.74% and 122.09%, respectively.

- In the models with  $B_w/B_h=0.94$ , displacement ductility increases by 69.66%, 89.49% and 85.13%, respectively, and curvature ductility changes by -11.36%, -36.20% and 120.32%, respectively.
- In the models with  $B_w/B_h=1.07$ , displacement ductility increases by 74.73%, 74.75% and 74.92%, respectively,

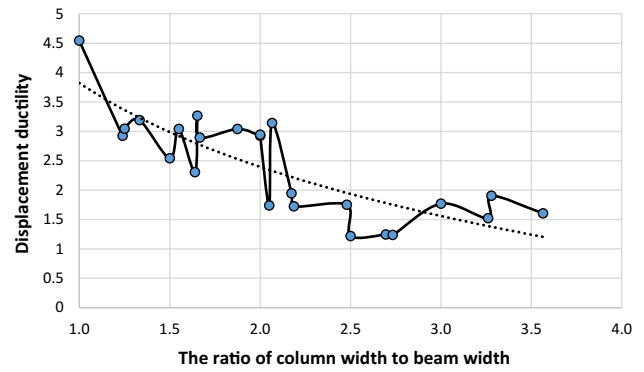


**Fig. 13** Displacement ductility of 24 numerical models

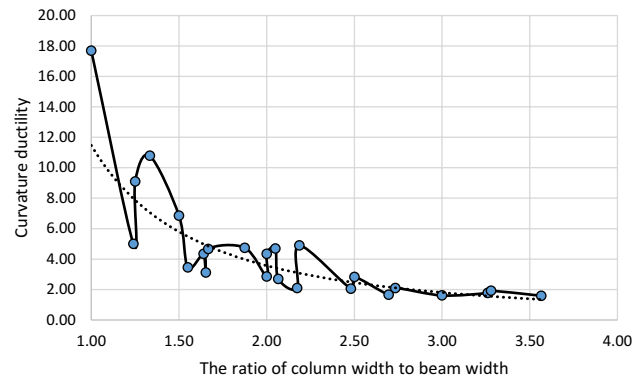


**Fig. 14** Diagram of curvature ductility of models

and curvature ductility alters by 0.95%, -26.57% and 93.52%, respectively.

- In the models with  $B_w/B_h=1.67$ , displacement ductility alters by 10.23%, 26.94% and 97.19%, respectively, and curvature ductility increases by 57.89%, 15.19% and 307.26%, respectively.

### 7.2 The Effect of Column Dimensions on Displacement Ductility and Curvature Ductility

To find the effect of  $C_w/C_h$  on the seismic response of RC joints, they are classified in six groups. Column dimensions were changed in each group, while beam dimensions remained constant. Based on the numerical results, by increasing the ratio of  $C_w/C_h$ , displacement ductility decreases due to the decrease of column stiffness in  $x$ -direction. The other important point is that, by increasing the ratio of  $C_w/C_h$ , both the curvature ductility and displacement ductility decrease. The proportions of the changes are presented below.

When the ratio of  $C_w/C_h$  increases by 54.12%, 129.36% and 169.43%:

- In the models with  $B_w/B_h=0.35$ , the displacement ductility decreases by  $-36.07\%$ ,  $-21.84\%$  and  $-17.51\%$ , respectively. Curvature ductility decrease, respectively, by  $-20.69\%$ ,  $-15.62\%$  and  $-24.40\%$ .
- In the models with  $B_w/B_h=0.42$ , the displacement ductility decreases by  $-40.47\%$ ,  $-39.85\%$  and  $-35.33\%$ , respectively. Curvature ductility decreases, respectively, by  $-27.76\%$ ,  $-43.57\%$  and  $-32.62\%$ .
- In the models with  $B_w/B_h=0.6$ , the displacement ductility alters by  $8.61\%$ ,  $-57.88\%$  and  $-57.35\%$ , respectively. Curvature ductility decreases, respectively, by  $-42.03\%$ ,  $-39.28\%$  and  $-54.97\%$ .
- In the models with  $B_w/B_h=0.94$ , the displacement ductility changes by  $2.36\%$ ,  $-8.35\%$  and  $-45.98\%$ , respectively. Curvature ductility decreases, respectively, by  $-71.04\%$ ,  $-59.77\%$  and  $-54.61\%$ .
- In the models with  $B_w/B_h=1.07$ , the displacement ductility decreases by  $-0.10\%$ ,  $-0.11\%$  and  $-42.83\%$ , respectively. Curvature ductility decreases, respectively, by  $-62.06\%$ ,  $-47.83\%$  and  $-48.32\%$ .
- In the models with  $B_w/B_h=1.67$ , the displacement ductility decreases by  $-35.62\%$ ,  $44.10\%$  and  $-49.29\%$ , respectively. Curvature ductility decreases, respectively, by  $-71.72\%$ ,  $-61.23\%$  and  $-75.45\%$ .

### 7.3 The Effect of $\rho_{col}$ on Displacement Ductility and Curvature Ductility

To evaluate the influence of  $\rho_{col}$  on the FE results, numerical models with the same beam dimensions are compared together. According to the analytical results, by increasing  $\rho_{col}$  (or decreasing  $A_{col}$ ), both the displacement ductility and curvature ductility decrease. The numerical changes in displacement ductility and curvature ductility are presented below.

When the  $\rho_{col}$  increases by  $0.17\%$ ,  $0.26\%$  and  $2.22\%$ :

- In the models with the  $B_w/B_h=0.35$ , displacement ductility decreases by  $-17.51\%$ ,  $-36.08\%$  and  $-21.83\%$ , respectively. The curvature ductility also decreases by  $-24.40\%$ ,  $-20.69\%$  and  $-15.62\%$ , respectively.
- In the models with the  $B_w/B_h=0.42$ , displacement ductility decreases by  $-35.33\%$ ,  $-40.47\%$  and  $-39.85\%$ , respectively. The curvature ductility also decreases by  $-32.62\%$ ,  $-27.76\%$  and  $-43.57\%$ , respectively.
- In the models with the  $B_w/B_h=0.60$ , displacement ductility changes by  $-57.35\%$ ,  $-8.61\%$  and  $-57.88\%$ , respectively. The curvature ductility also decreases by  $-54.97\%$ ,  $-42.03\%$  and  $-39.27\%$ , respectively.
- In the models with the  $B_w/B_h=0.94$ , displacement ductility increases by  $85.13\%$ ,  $89.49\%$  and  $69.67\%$ , respectively. The curvature ductility also changes by  $120.32\%$ ,  $-36.20\%$  and  $-11.36\%$ , respectively.

- In the models with the  $B_w/B_h=1.07$ , displacement ductility decreases by  $-42.83\%$ ,  $-0.1\%$  and  $-0.11\%$ , respectively. The curvature ductility also decreases by  $-48.33\%$ ,  $-62.06\%$  and  $-47.83\%$ , respectively.
- In the models with the  $B_w/B_h=1.67$ , displacement ductility decreases by  $-49.29\%$ ,  $-35.62\%$  and  $-44.09\%$ , respectively. The curvature ductility also decreases by  $-75.45\%$ ,  $-71.71\%$  and  $-61.23\%$ , respectively.

### 7.4 The Effect of Beam Dimension on Displacement Ductility and Curvature Ductility

To investigate the effect of beam dimensions on the FE outcomes, the beam dimensions were changed, while the column dimensions remained constant. The FE analysis outcomes indicated that by increasing the ratio of  $B_w/B_h$ , both displacement ductility and curvature ductility increase. The proportions of their changes are mentioned below:

When the ratio of  $B_w/B_h$  increases by  $17.75\%$ ,  $69.56\%$ ,  $164.95\%$ ,  $201.45\%$  and  $371.01\%$ :

- In the models with  $C_w/C_h=1.09$ , the displacement ductility increases by  $51.22\%$ ,  $48.74\%$ ,  $63.98\%$ ,  $56.45\%$  and  $133.47\%$ , respectively. Curvature ductility increases, respectively, by  $35.76\%$ ,  $121.66\%$ ,  $413.03\%$ ,  $332.45\%$  and  $741.56\%$ .
- In the models with  $C_w/C_h=1.68$ , the displacement ductility increases by  $40.81\%$ ,  $152.73\%$ ,  $162.53\%$ ,  $144.52\%$  and  $135.14\%$ , respectively. Curvature ductility increases, respectively, by  $23.66\%$ ,  $62.00\%$ ,  $87.32\%$ ,  $106.88\%$  and  $200.11\%$ .
- In the models with  $C_w/C_h=2.5$ , the displacement ductility changes by  $37.00\%$ ,  $-19.84\%$ ,  $92.28\%$ ,  $99.95\%$  and  $66.99\%$ , respectively. Curvature ductility changes, respectively, by  $-9.21\%$ ,  $59.51\%$ ,  $144.62\%$ ,  $167.36\%$  and  $286.64\%$ .
- In the models with  $C_w/C_h=2.93$ , the displacement ductility alters by  $18.55\%$ ,  $-23.10\%$ ,  $7.38\%$ ,  $8.43\%$  and  $43.34\%$ , respectively. Curvature ductility increases, respectively, by  $21.00\%$ ,  $32.01\%$ ,  $208.03\%$ ,  $195.60\%$  and  $173.34\%$ .

## 8 Conclusion

This study presents the effect of beam and column dimensions on seismic behavior of RC wide column–beam joints. Twenty-four numerical models with different beam and column dimensions were developed and analyzed in nonlinear finite element software. Concrete damage plasticity theory was used in the finite element software. In addition, the influence of mesh size on the FE analysis was investigated.

According to obtained results and evaluations, following conclusions can be drawn:

- When the beam dimensions are constant, by decreasing the ratio of  $C_w/B_w$  displacement ductility fluctuates: when  $B_w/B_h \geq 0.6$  displacement ductility increases, while it decreases when  $B_w/B_h \leq 0.42$ .
- By decreasing the  $C_w/B_w$  when the beam dimensions are constant, curvature ductility increases.
- When the beam dimensions are constant, by increasing the ratio of  $C_w/C_h$ , both displacement ductility and curvature ductility decrease.
- When the column dimensions are constant, when the ratio of  $B_w/B_h$  increases, both displacement ductility and curvature ductility increase.
- When the beam dimensions remain constant, by increasing the  $\rho_{col}$ , both displacement ductility and curvature ductility decrease.
- Mesh size of elements affect the FE analysis considerably and the best mesh size in this study was 65 mm.

**Funding** Not applicable.

## References

1. Benavent-Climent A, Cahís X, Zahran R (2009) Exterior wide beam–column connections in existing RC frames subjected to lateral earthquake loads. *Eng Struct* 31(7):1414–1424. <https://doi.org/10.1016/j.engstruct.2009.02.008>
2. Alva GMS, ALH de Cresce El Debs (2013) Moment–rotation relationship of RC beam–column connections: experimental tests and analytical model. *Eng Struct* 56:1427–1438. <https://doi.org/10.1016/j.engstruct.2013.07.016>
3. Lee J-Y, Kim J-Y, Oh G-J (2009) Strength deterioration of reinforced concrete beam–column joints subjected to cyclic loading. *Eng Struct* 31(9):2070–2085. <https://doi.org/10.1016/j.engstruct.2009.03.009>
4. Li B, Lam ES, Wu B, Wang Y (2013) Experimental investigation on reinforced concrete interior beam–column joints rehabilitated by ferrocement jackets. *Eng Struct* 56:897–909. <https://doi.org/10.1016/j.engstruct.2013.05.038>
5. Behnam H, Kuang JS (2018) Exterior RC wide beam–column connections: effect of spandrel beam on seismic behavior. *J Struct Eng* 144(4):04018013. [https://doi.org/10.1061/\(asce\)st.1943-541x.0001995](https://doi.org/10.1061/(asce)st.1943-541x.0001995)
6. Siah WL, Stehle JS, Mendis P, Goldsworthy H (2003) Interior wide beam connections subjected to lateral earthquake loading. *Eng Struct* 25(3):281–291. [https://doi.org/10.1016/s0141-0296\(02\)00150-5](https://doi.org/10.1016/s0141-0296(02)00150-5)
7. Ehsani MR, Wight JK (1985) Effect of transverse beams and slab on behavior of reinforced concrete beam-to-column connections. *ACI J Proc*. <https://doi.org/10.14359/10327>
8. LaFave JM, Wight JK (1999) Reinforced concrete exterior wide beam–column–slab connections subjected to lateral earthquake loading. *ACI Struct J*. <https://doi.org/10.14359/694>
9. Fadwa I, Ali TA, Nazih E, Sara M (2014) Reinforced concrete wide and conventional beam–column connections subjected to lateral load. *Eng Struct* 76:34–48. <https://doi.org/10.1016/j.engstruct.2014.06.029>
10. Mirzabagheri S, Tasnimi AA, Mohammadi MS (2016) Behavior of interior RC wide and conventional beam–column roof joints under cyclic load. *Eng Struct*. <https://doi.org/10.1016/j.engstruct.2015.12.011>
11. Yousef YS, Chemrouk M (2012) Curvature ductility factor of rectangular sections reinforced concrete beams. *Int J Civ Environ Eng* 6(11):971–976
12. Li B, Wu Y, Pan TC (2002) Seismic behavior of nonseismically detailed interior beam-wide column joints—Part I: experimental results and observed behavior. *ACI Struct J*. <https://doi.org/10.14359/12344>
13. Li B, Wu Y, Pan TC (2003) Seismic behavior of nonseismically detailed interior beam-wide column joints—Part II: theoretical comparisons and analytical studies. *ACI Struct J*. <https://doi.org/10.14359/12439>
14. Li B, Pan TC, Tran CNT (2009) Seismic behavior of nonseismically detailed interior beam-wide column and beam-wall connections. *ACI Struct J*. <https://doi.org/10.14359/51663099>
15. B Li, HY Grace Chua (2008) Rapid repair of earthquake damaged RC interior beam-wide column joints and beam-wall joints using FRP composites. *Key Eng Mater* 400–402:491–499. <https://doi.org/10.4028/www.scientific.net/kem.400-402.491>
16. Lu X, Urukup TH, Li S, Lin F (2012) Seismic behavior of interior RC beam–column joints with additional bars under cyclic loading. *Earthq Struct* 3(1):37–57. <https://doi.org/10.12989/eas.2012.3.1.037>
17. Omidi M, Behnamfar F (2015) A numerical model for simulation of RC beam–column connections. *Eng Struct* 88:51–73. <https://doi.org/10.1016/j.engstruct.2015.01.025>
18. Elsouri AM, Harajli MH (2015) Interior RC wide beam–narrow column joints: potential for improving seismic resistance. *Eng Struct* 99:42–55. <https://doi.org/10.1016/j.engstruct.2015.04.020>
19. Najafgholipour MA, Dehghan SM, Dooshabi A, Niroomandi A (2017) Finite element analysis of reinforced concrete beam–column connections with governing joint shear failure mode. *Lat Am J Solids Struct* 14(7):1200–1225. <https://doi.org/10.1590/1679-78253682>
20. Behnam H, Kuang JS, RYC Huang (2017) Exterior RC wide beam–column connections: effect of beam width ratio on seismic behaviour. *Eng Struct* 147:27–44. <https://doi.org/10.1016/j.engstruct.2017.05.044>
21. Behnam H, Kuang JS, Samali B (2018) Parametric finite element analysis of RC wide beam–column connections. *Comput Struct* 205:28–44. <https://doi.org/10.1016/j.compstruc.2018.04.004>
22. Genikomsou A, Polak MA (2016) Damaged plasticity modeling of concrete in finite element analysis of reinforced concrete slabs. In: Proceedings of the 9th international conference on fracture mechanics of concrete and concrete structures. <https://doi.org/10.21012/fc9.006>
23. Chaudhari SV, Chakrabarti MA (2012) Modeling of concrete for nonlinear analysis using finite element code ABAQUS. *Int J Comput Appl* 44(7):14–18. <https://doi.org/10.5120/6274-8437>
24. Lee J, Fenves GL (August 1998) Plastic-damage model for cyclic loading of concrete structures. *J Eng Mech* 124(8):892–900. [https://doi.org/10.1061/\(asce\)0733-9399\(1998\)124:8\(892\)](https://doi.org/10.1061/(asce)0733-9399(1998)124:8(892))
25. Abaqus Analysis User’s Manual 6.10. Dassault Systèmes Simulia Corp., Providence, RI, USA
26. Oller S, Oñate E, Oliver J, Lubliner J (1990) Finite element nonlinear analysis of concrete structures using a ‘plastic-damage model’. *Eng Fract Mech* 35(1–3):219–231. [https://doi.org/10.1016/0013-7944\(90\)90200-z](https://doi.org/10.1016/0013-7944(90)90200-z)
27. Lubliner J, Oliver J, Oller S, Oñate E (1989) A plastic-damage model for concrete. *Int J Solids Struct* 25(3):299–326. [https://doi.org/10.1016/0020-7683\(89\)90050-4](https://doi.org/10.1016/0020-7683(89)90050-4)



28. Yazdani S, Schreyer HL (1990) Combined plasticity and damage mechanics model for plain concrete. *J Eng Mech* 116(7):1435–1450
29. Jankowiak T, Łodygowski T (2014) Plasticity conditions and failure criteria for quasi-brittle materials. *Handb Damage Mech*. [https://doi.org/10.1007/978-1-4614-5589-9\\_48](https://doi.org/10.1007/978-1-4614-5589-9_48)
30. Birtel V, Mark P (2006) Parameterised finite element modelling of RC beam shear failure. In: ABAQUS users' conference, pp 95–108.A
31. Belarbi A, Hsu TTC (1994) Constitutive laws of concrete in tension and reinforcing bars stiffened by concrete. *ACI Struct J*. <https://doi.org/10.14359/4154>
32. Genikomsou AS, Polak MA (2015) Finite element analysis of punching shear of concrete slabs using damaged plasticity model in ABAQUS. *Eng Struct* 98:38–48. <https://doi.org/10.1016/j.engstruct.2015.04.016>
33. Wang PS, Vecchio FJ (2006) *VecTor2 and formworks user manual*. University of Toronto, Canada
34. Park R, Paulay T (1975) *Reinforced concrete structures*. Wiley. Available from <https://doi.org/10.1002/9780470172834>
35. Lam SSE, Wu B, Wong YL, Wang ZY, Liu ZQ, Li CS (2003) Drift capacity of rectangular reinforced concrete columns with low lateral confinement and high-axial load. *J Struct Eng* 129(6):733–742. [https://doi.org/10.1061/\(asce\)0733-9445\(2003\)129:6\(733\)](https://doi.org/10.1061/(asce)0733-9445(2003)129:6(733))